Table 1
Computational conditions

Heart rate	0.87 Hz (52 beat/min)
Cardiac cycle T	1.15 s
Cardiac output	9.17×10^{-5} m^3/s (5.5 l/min)
Entrance flow	6.42×10^{-5} m^3/s (3.85 l/min)
Average velocity at maximum flow rate $u'_{\max}$	0.74 m/s
Entrance vessel diameter D	28.25×10^{-3} m
Kinematic viscosity ν	4.0×10^{-6} m^2/s

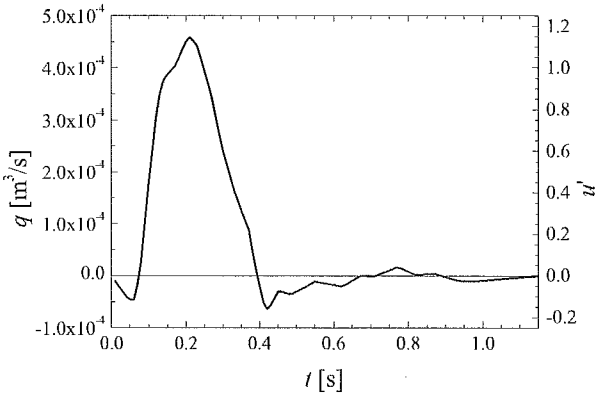

Fig. 5. Time variation of flow volume in descending aorta and of cross-sectional average flow velocity at upstream boundary.

3. Numerical simulation of correction of aliasing

3.1. Formulation

In this section, we investigate the effectiveness of the proposed method to detect and correct the aliasing signal using the feedback intensity in UMI simulation. For that purpose, we carry out UMI simulation using a simple two-dimensional model problem for blood flow in the descending aorta with an aneurysm. The shape of blood vessel is obtained by transesophageal ultrasonography with an ultrasound device (SONOS 5500, Philips Medical Systems, Andover, MA, USA) with transesophageal ultrasonic transducer (T6210, Philips Medical Systems, Andover, MA, USA). Table 1 summarizes parameters used in this computation. Among them, heart rate and cardiac output are measured during the ultrasonic measurement. Cardiac cycle T is calculated from the heart rate. The upstream shape of the blood vessel is assumed to be cylindrical in order to determine two-dimensional inlet velocity profile according to the three-dimensional time varying flow rate data, and the diameter D is calculated from the image. We assume that 30% of the cardiac output flows into the branches and that the remaining 70% (6.42×10^{-5} m^{3}s^{-1}) flows into the descending aorta referring to the blood flow measurement data [18]. The variation of the flow rate q is modeled as shown in Fig. 5 according to the MR measurement by Olufsen et al. [19]. Blood is assumed to be a Newtonian fluid with density $\rho = 1.00 \times 10^3$ kgm^{-3} and dynamic viscosity $\mu = 4.0 \times 10^{-3}$ Pas.

All the values are nondimensionalized with the diameter of the blood vessel D, the cross-sectional average velocity $u_{\max}$ at the upstream boundary for the maximum cardiac output, and the kinematic vis-

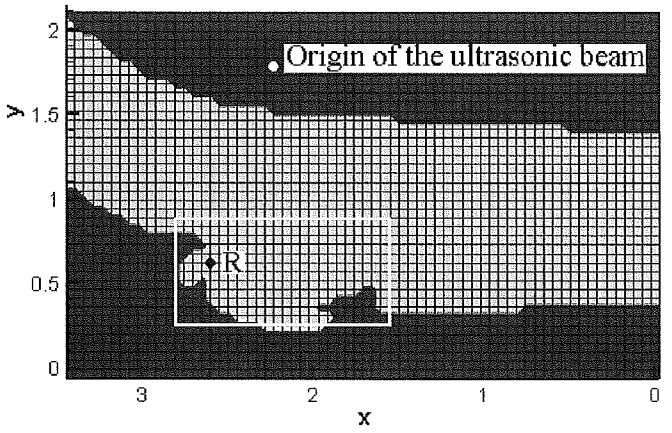

Fig. 6. Computational grid and monitoring region in which monitoring points for feedback are arranged.

cosity ν of the blood. From here on, the same symbols are used for both dimensional and nondimensional values without confusion.

In order to define a two-dimensional computational domain, the B-mode image of the blood vessel obtained by ultrasonic diagnostic equipment is digitized to extract the cross-sectional surface manually, and the pixel data is allocated in a staggered grid system with uniform grid spacing as shown in Fig. 6. In this research, we introduce a grid of 65 $\times$ 40 points in x and y directions with grid spacing of 1.487 $\times$ 10^{-3} m in each direction, compromising between the reproducibility of the vessel shape and the computational time. The origin of the ultrasonic beam, where ultrasound is emitted from the probe, is set at the same position as the measurement [see the center of a sector in Fig. 1(a)].

First, we perform a numerical simulation to obtain a standard solution, or a model of real blood flow. The velocity profile at the upstream boundary in calculating the standard solution was determined from a three-dimensional steady blood flow simulation in the extended blood vessel consisting of ascending aorta, aortic arch, descending aorta and abdominal aorta with commercial computational fluid dynamics software (FLUENT 6.1.22, Fluent Inc., Lebanon, NH, USA). In the steady numerical simulation with FLUENT, inflow velocity is set at 20 cms^{-1}, which is the mean value of blood velocity in the aorta. At the downstream boundary of the standard solution, a free-flow condition ($\partial/\partial n = 0$, n: coordinate normal to the boundary) is applied, and a no-slip condition is applied to the blood vessel wall. The adequate residual at convergence and the maximum iteration number are respectively determined as 1 $\times$ 10^{-5} and 300 after test computations. It is noted that the condition to obtain the standard solution is the same as that of the former paper [11] except that Poiseuille flow is assumed at the entrance in the previous study. In this paper, we apply the other velocity profile as shown in Fig. 7 at each time step in order to calculate under more realistic condition. After the computation of the standard solution, aliasing is artificially introduced in the standard solution, setting the threshold values, $V_{\max}$ and $V_{\min}$, and processing all Doppler velocity data not to excess the threshold vales in manner of wraparound the Doppler velocity scale.

For UMI simulation, the uniform velocity profile is applied at the upstream boundary. The other computational conditions are the same as that of the standard solution. In the UMI simulation, discrepancy caused by the incorrect upstream boundary condition is compensated for by the feedback action and the result approaches that of the standard solution in the region of feedback. In this study, we define the rectangular arrangement of monitoring points for the feedback covering the aneurysm which consists of all 325 points in the white rectangular region as shown in Fig. 6 to reproduce the blood flow in the region.

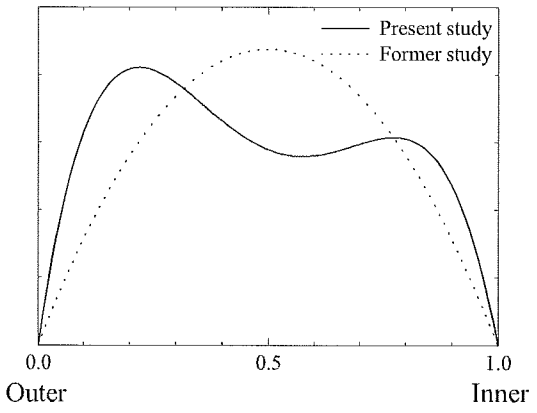

Fig. 7. The x-directional velocity profile at the upstream boundary.

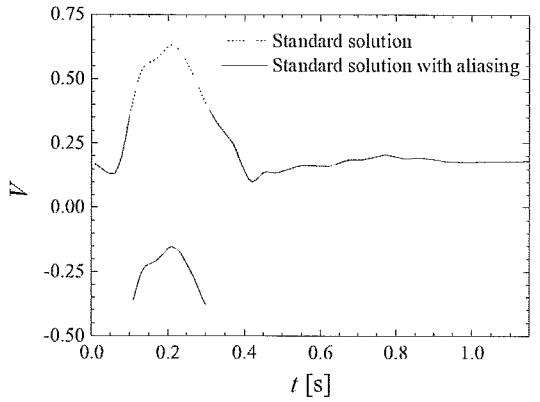

Fig. 8. Variation of Doppler velocity of nonaliased or aliased standard solution at monitoring point R.

The representative monitoring point R, where the aliasing is observed in the aliased standard solution, is also chosen in the monitoring region to observe the variation of any variables.

3.2. Results and discussion

The numerical simulation to obtain the standard solution takes more than 26 cardiac cycles to converge to the periodic oscillation. We define the standard solution as the repetition of the result in the 26th cardiac cycle. Figure 8 shows Doppler velocity of the standard solution at point R (see Fig. 6).

First, we investigated the detection of the aliasing. Based on the method described in previous section, we artificially introduce aliasing for this standard solution. In this study, the threshold values of Doppler velocity, $V_{\max}$ and $V_{\min}$, are set $\pm$ 25 cms^{-1} (0.392 in the nondimensional value). In Fig. 8, horizontal lines mean the nondimensional threshold values.

Figure 9(a) shows three snapshots of the color Doppler image in the monitoring region (white rectangular region in Fig. 6) in one cardiac cycle for the standard solution in which aliasing is introduced. In the preceding two images, the aliasing can be observed. The regions where the aliasing is introduced are shown with volume rendering in Fig. 9(b). The blue regions mean the exceeding the upper threshold value, the red region means below the lower threshold value, and the green lines mean the vessel wall.

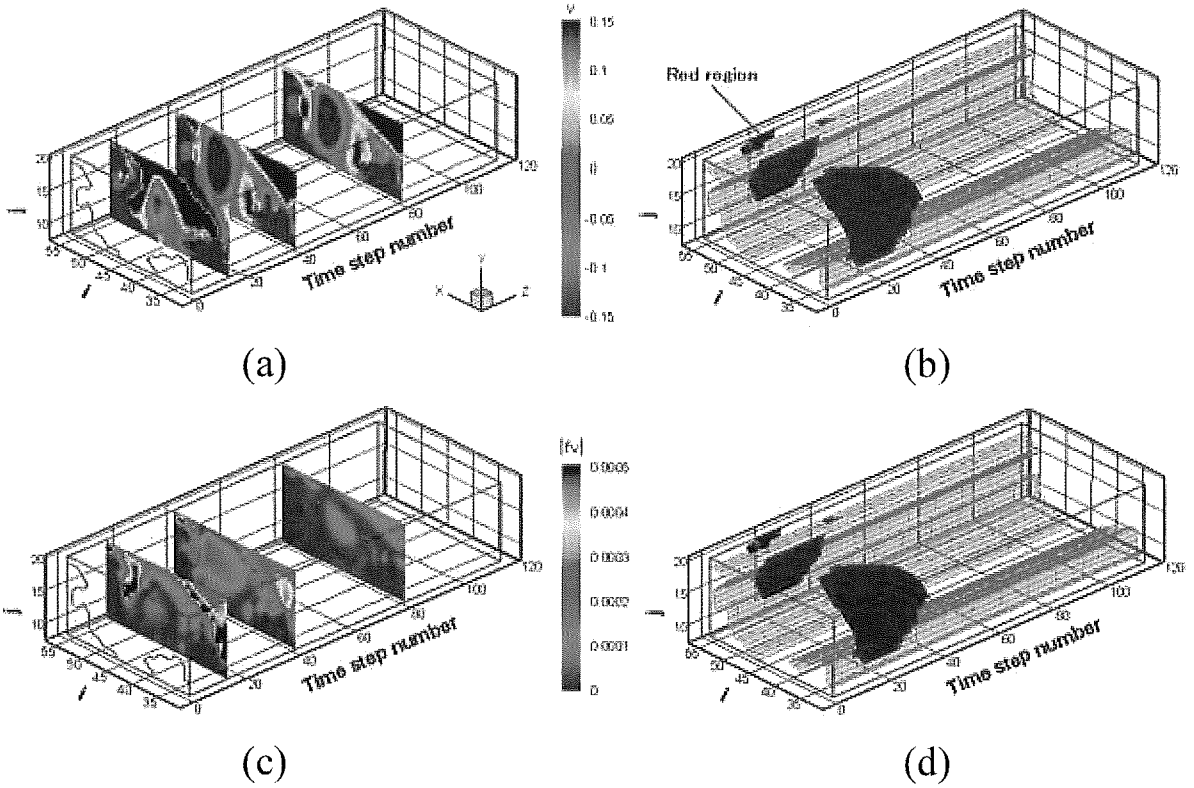

Fig. 9. Distribution of variables in the monitoring region in one cardiac cycle: (a) color Doppler images at $t = 0.15$ s in acceleration phase, and $t = 0.40$ s and 0.80 s in deceleration phase, (b) volume rendering of aliasing region, (c) feedback intensity in the first cardiac cycle of UMI simulation using aliased standard solution at the same timing as that of (a), and (d) volume rendering of the region where aliasing is detected by UMI simulation with correction B.

In the vicinity of the time step number 21 ($t = 0.21$ s) at which maximum flow rate occurs, the aliasing regions spread in the upstream and downstream area of the monitoring region.

The UMI simulation is performed using the aliased standard solution. The optimum combination of gains (K_v, K_p) is determined as (0.4, 0.4) to minimize the average error norms $\bar{e}_N(\mathrm{u})$ of the velocity vector based on the result of the former research [11]. All UMI simulations described below are carried out with these values of gains. The instantaneous feedback intensity $|f_v|$, which is the average absolute value of the artificial force f_v during a time step in the first cardiac cycle as shown in Fig. 9(c) becomes relatively high in the region where aliasing occurs in Fig. 9(a). By using this unnatural feedback signal as the index of the aliasing, we performed UMI simulation with correction. The area where the aliasing is detected by UMI simulation with correction B is shown in Fig. 9(d). Figure 9(d) completely agrees with Fig. 9(b), implying that all aliasing introduced regions are detected correctly.

Correction of aliasing in UMI simulation is evaluated as follows. Color Doppler image of the nonaliased and aliased standard solution at peak flow ($t = 0.21$ s) are shown in Fig. 10. Here, note that the maximum and minimum values of the color bar do not correspond to $V_{\max}$ and $V_{\min}$, respectively, to emphasize the difference in the color Doppler images clearly. Corresponding color Doppler images of UMI simulations are shown in Fig. 11. Figure 11(a) shows the color Doppler image obtained without feedback of UMI simulation (ordinary simulation), and Fig. 11(b) and (c) show those of UMI simulations without correction of aliasing and with correction B, respectively. Since the applied upstream boundary

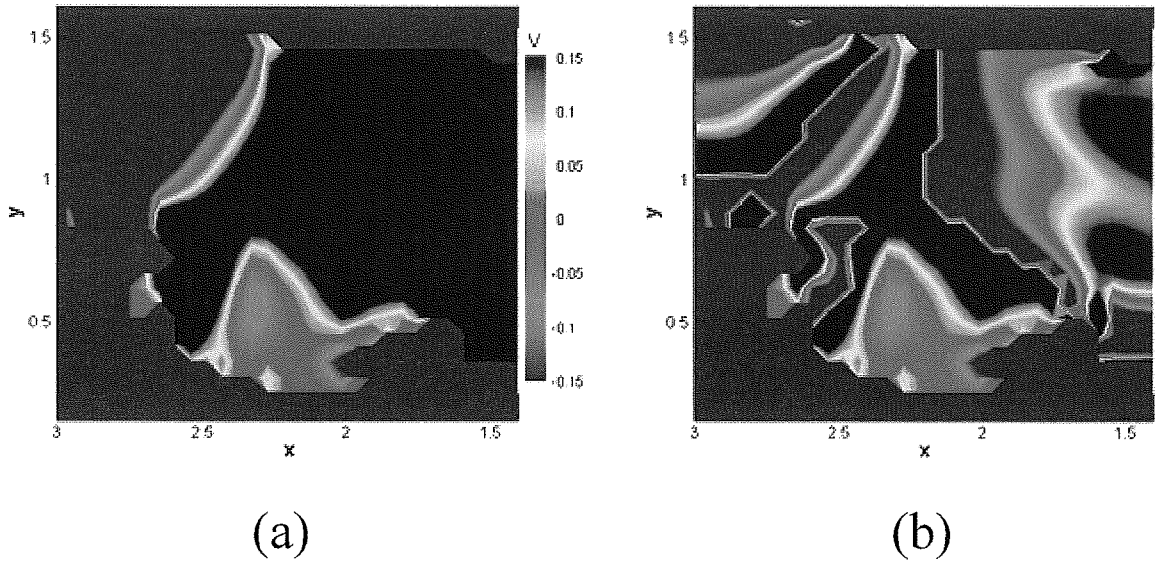

Fig. 10. Comparison of (a) color Doppler image around an aneurysm at peak flow of standard solution without aliasing and (b) that with aliasing.

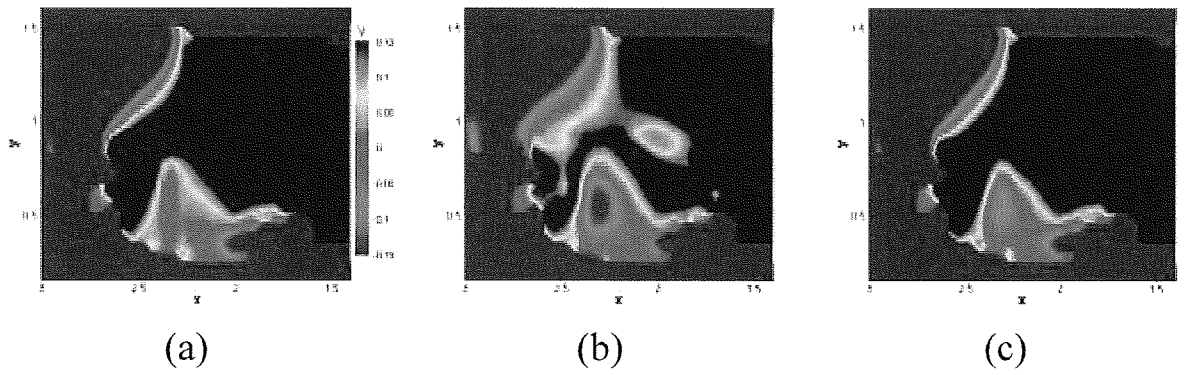

Fig. 11. Comparison of (a) color Doppler image around an aneurysm at peak flow of UMI simulation without feedback (ordinary simulation), and (b) and (c) those of UMI simulations without correction of aliasing and with correction B, respectively.

condition is not so different between the standard solution and UMI simulations, Figs 10(a) and 11(a) are similar to each other, but the different color pattern is visible in the aneurysm. The color Doppler image of UMI simulation without correction at peak flow [Fig. 11(b)] shows an erroneous result. In contrast, UMI simulation with correction B [Fig. 11(c)] correctly reproduces the standard solution [Fig. 10(a)]. The result of UMI simulation with correction A is similar to that of correction B showing good agreement with the standard solution, although it is omitted here because of page limitation.

Variation of the velocity components and the pressure at point R in one cardiac cycle is shown in Fig. 12. The velocity components of the ordinary simulation with dotted line are different from those of the standard solution with bold line. UMI simulations with correction A and B, which almost overlap each other, closely converges to the standard solution, while the UMI simulation without correction shows the result completely different from those of the standard solution and even worse than the

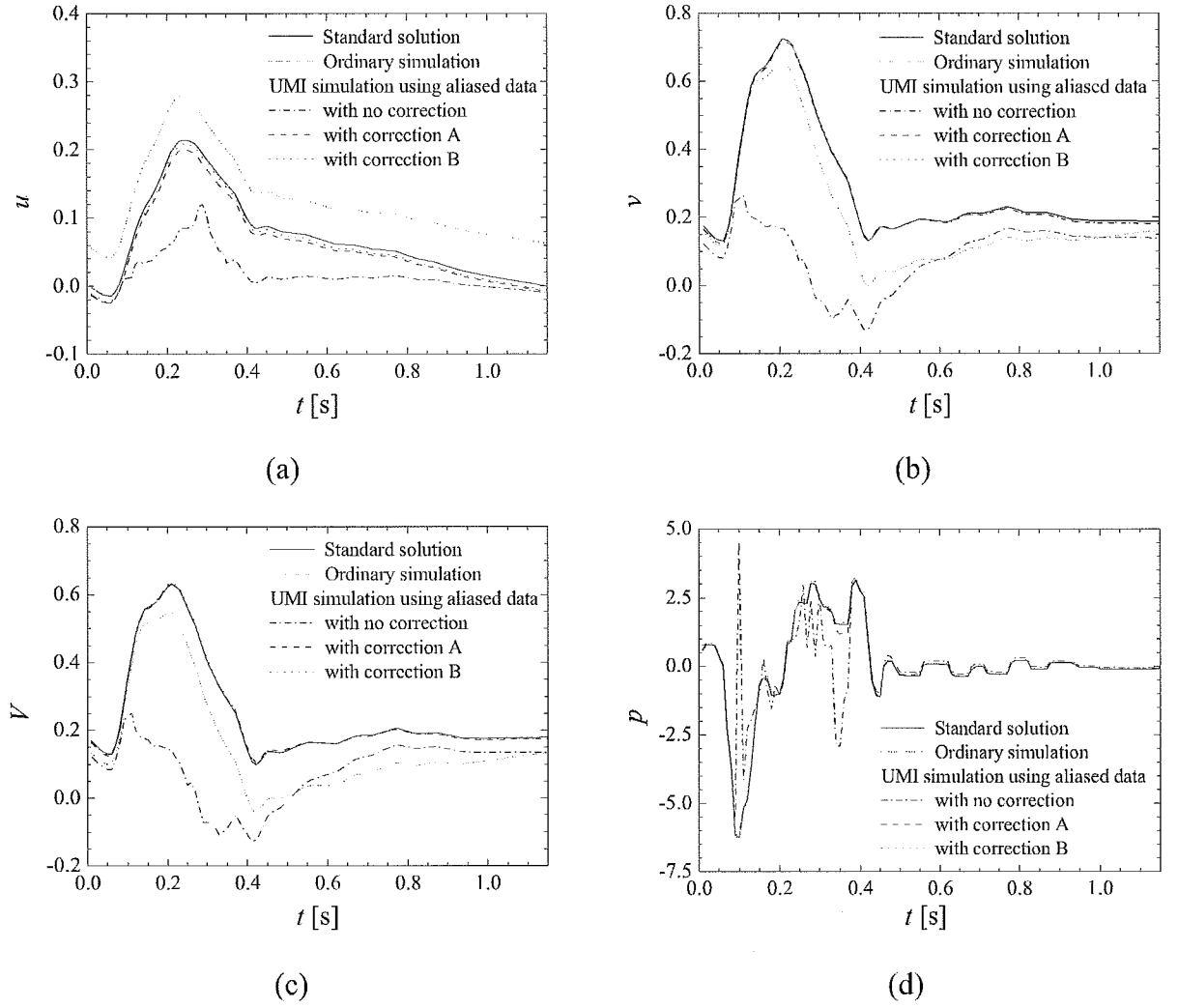

Fig. 12. Comparison of periodic solutions of (a) x-directional velocity u, (b) y-directional velocity v, (c) Doppler velocity V, and (d) pressure p at monitoring point R. The UMI simulations used the aliased standard solution.

ordinary simulation. At the point R where the results are observed, the aliasing occurs from $t = 0.11$ s to 0.30 s. However, the timing when the error against the standard solution enlarges is earlier than $t = 0.11$ s. This is because the result at the point R is affected by the aliasing data which is fed back to UMI simulation at the other monitoring points. The influence of the aliasing on the result is also observed at the other monitoring points where aliasing does not occur through one cardiac cycle, skewing the velocity components from those of the standard solution and perturbing the pressure.

For the quantitative comparison between these results, the average error norms calculated by Eq. (7) are summarized in Table 2. The UMI simulation using aliasing data with no correction does not improve the computational accuracy comparing to those of the ordinary simulation. On the other hand, the results of UMI simulations with corrections A and B improve the computational accuracy about the velocity vectors. Correction A is simple to apply and provides results similar to that of correction B. It is noted that UMI simulation with correction B gives the result exactly the same as that of the UMI simulation with

Table 2
Comparison of average error norm

	u	v	V	p
Standard solution	0	0	0	0
Ordinary simulation	1	1	1	1
UMI simulation using aliased data				
– with no correction	2.758	1.625	1.373	29.086
– with correction A	0.447	0.212	0.180	1.787
– with correction B	0.369	0.162	0.136	1.031
UMI simulation using nonaliased data	0.369	0.162	0.136	1.031

the nonaliased standard solution, which is the best result in UMI simulation in terms of the reproduction of the standard solution. The errors in the velocity components are reduced by the application of UMI simulation to 37% for u, 16% for v, and 14% for V of those of the ordinary simulation. Here, the accuracy of the y-directional velocity component v is more improved than the x-directional velocity component u since the origin of the ultrasonic beam is located in the y-direction of the monitoring region, and therefore, Doppler velocity V includes more information of v than u. In contrast, though the error of the pressure becomes large when UMI simulation is carried out, it is not a crucial problem because those values are very small as seen in Fig. 12(d).

In the present model problem, aliasing can be detected from the instantaneous feedback signal f_v in UMI simulation, and aliasing can be corrected with two correction methods. Considering the false recognition of the fully disturbed flow as the aliasing or the effect of the other artifacts, UMI simulation with correction B may lead incorrect results due to its correction process. On the other hand, UMI simulation with correction A only prevents all suspect data from being introduced into UMI simulation, and there is no possibility that the application of feedback contrary lead UMI simulation to the incorrect results. Hence, correction A can be thought to give a more robust method useful for practical applications.

4. Conclusions

In this paper we investigated the detection and the correction of aliasing of ultrasonic blood velocity measurement in Ultrasonic-Measurement-Integrated (UMI) simulation. A UMI simulation was performed for a two-dimensional model problem using a standard numerical solution with and without artificially introduced aliasing. Aliasing causes UMI simulation to differ from the standard solution and the error may be greater than that of ordinary simulations. The artificial force in the feedback of UMI simulation can be used as an excellent index to detect the aliasing. We proposed two ways for the correction of the aliasing: correction A, in which measurement velocity is replaced with the computational one at the monitoring point where the aliasing is detected, substantially improves the accuracy of UMI simulation; and correction B, in which measurement velocity is replaced with an estimated Doppler velocity at the point, can provide the same result as that of UMI simulation using the nonaliased standard solution. Though correction B yields the most accurate result, correction A seems more robust and, therefore, a beneficial choice considering the other artifacts in the measurement. The present study revealed the potential of UMI simulation to improve the accuracy of the original ultrasonic measurement. For future work, we will extend the proposed method to three-dimensional problems and the application to the real color Doppler ultrasonography in order to develop advanced medical diagnostic and treatment equipment.

Acknowledgements

The present study was supported in part by the Research Fellowships of the Japan Society for the Promotion of Science for Young Scientists #16-3421. The authors would like to thank Assistant Professor N. Asai of the University of Aizu for his assistance in grid generation for the computation with FLUENT. The computations were performed using the supercomputer system SGI ORIGIN 2000 in the Advanced Fluid Information Research Center, Institute of Fluid Science, Tohoku University. The authors are grateful to the staff of the AFI Research Center for their support in the computational work.

References

[1] C.G. Caro, J.M. Fitz-Gerald and R.C. Schroter, Atheroma and arterial wall shear. Observation, correlation and proposal of a shear-dependent mass transfer mechanism for atherogenesis, *Proc. R. Soc. Lond. B Biol. Soci.* **117** (1971), 109–159.
[2] D.N. Ku, D.P. Giddens, C.K. Zarins and S. Glagov, Pulsatile flow and atherosclerosis in the human carotid bifurcation. Positive correlation between plaque location and low oscillating shear stress, *Arteriosclerosis* **5** (1985), 293–302.
[3] D.P. Giddens, C.K. Zarins and S. Glagov, The role of fluid mechanics in the localization and detection of atherosclerosis, *J. Biomech. Eng.* **115** (1993), 588–594.
[4] H.S. Flora, B. Talei-Faz, L. Ansdell, E.J. Chaloner, A. Sweeny, A. Grass and M. Adiseshiah, Aneurysm wall shear stress and tendency to rupture are features of physical wall properties: an experimental study, *J. Endovasc. Ther.* **9** (2002), 665–675.
[5] D.A. Steinman, Image-based computational fluid dynamics modeling in realistic arterial geometries, *Ann. Biomed. Eng.* **30** (2002), 483–497.
[6] Y. Liu, Y. Lai, A. Nagaraj, B. Kane, A. Hamilton, R. Greene, D.D. McPherson and K.B. Chandran, Pulsatile flow simulation in arterial vascular segments with intravascular ultrasound images, *Med. Eng. Phys.* **23** (2001), 583–595.
[7] I. Marshall, S. Zhao, P. Papathanasopoulou, P. Hoskins and X.Y. Xu, MRI and CFD studies of pulsatile flow in healthy and stenosed carotid bifurcation models, *J. Biomech.* **37** (2004), 679–687.
[8] E.S. Di Martino, G. Guadagni, A. Fumero, G. Ballerini, R. Spirito, P. Biglioli and A. Redaelli, Fluid-structure interaction within realistic three-dimensional models of the aneurysmatic aorta as a guidance to assess the risk of rupture of the aneurysm, *Med. Eng. Phys.* **23** (2001), 647–655.
[9] E.A. Finol and C.H. Amon, Blood flow in abdominal aortic aneurysms: pulsatile flow hemodynamics, *J. Biomech. Eng.* **123** (2001), 474–484.
[10] K. Ferrara and G. DeAngelis, Color flow mapping, *Ultrasound Med. Biol.* **23** (1997), 321–345.
[11] K. Funamoto, T. Hayase, A. Shirai, Y. Saijo and T. Yambe, Fundamental study of Ultrasonic-Measurement-Integrated simulation of real blood flow in the aorta, *Ann. Biomed. Eng.* **33** (2005), 413–426.
[12] K.R. Baek, M.H. Bae and S.B. Park, A new aliasing extension method for ultrasonic 2-dimensional pulsed Doppler systems, *Ultrason. Imaging* **11** (1989), 233–244.
[13] P. Fan, N.C. Nanda, R.P. Gatewood, Jr., E.G. Cape and A.P. Yoganathan, Transesophageal color Doppler evaluation of obstructive lesions using the new "Quasar" technology, *Ultrasound Med. Biol.* **21** (1995), 1021–1028.
[14] S.F.C. Stewart, Aliasing-tolerant color Doppler quantification of regurgitant jets, *Ultrasound Med. Biol.* **24** (1998), 881–898.
[15] T. Hayase and S. Hayashi, State estimator of flow as an integrated computational method with the feedback of online experimental measurement, *J. Fluids Eng.* **119** (1997), 814–822.
[16] T. Hayase, J.A.C. Humphrey and R. Greif, *Mini-manual for ROTFLO2*, Dept. Mech. Eng. Rep. FM-90-1, Univ. Calif. Berkeley, 1990.
[17] S.V. Patankar, *Numerical Heat Transfer and Fluid Flow*, Hemisphere Pub. Corp.,Washington DC/New York, 1980.
[18] W.F. Ganong, *Review of Medical Physiology*, (17th ed.), Appleton & Lange, Norwalk, 1995, p. 555.
[19] M.S. Olufsen, C.S. Peskin, W.Y. Kim, E.M. Pedersen, A. Nadim and J. Larsen, Numerical simulation and experimental validation of blood flow in arteries with structured-tree outflow conditions, *Ann. Biomed. Eng.* **28** (2000), 1281–1299.

J Med Ultrasonics (2005) 32:91–99
DOI 10.1007/s10396-005-0041-3

ORIGINAL ARTICLE

Esmeraldo dos SANTOS FILHO
Makoto YOSHIZAWA · Akira TANAKA
Yoshifumi SAIJO · Takahiro IWAMOTO

Moment-based texture segmentation of luminal contour in intravascular ultrasound images

Received: December 26, 2004 / Accepted: April 4, 2005

Abstract
Purpose. A system for luminal contour segmentation in intravascular ultrasound images is proposed.
Methods. Moment-based texture features are used for clustering of the pixels in the input image. After the clustering, morphological smoothing and a boundary detection process are applied and the final image is obtained.
Results. The proposed method was applied to 15 images from different patients, and a correlation coefficient of 0.86 was obtained between the areas of lumen automatically and manually defined.
Conclusion. Moment-based texture features together with the radial feature are powerful tools for identification of the lumen region in intravascular ultrasound images. Morphological filtering was useful for improving the segmentation results.

Keywords ultrasound · texture · image segmentation

Introduction

Cardiovascular pathologies are one of the main causes of mortality in the Western world. Atherosclerosis, a disease of the intima layer of the artery, represents the essential characteristic of arterial pathologies.[1] Atherosclerosis consists of lipids, complex carbohydrates, blood cells, fibrous tissues, and calcified deposits forming a plaque that occludes progressively the lumen of the artery. When occurring within coronary arteries, the consequences of this pathology can be dramatic, such as myocardial infarct, because the function of these arteries is to irrigate the cardiac muscle.[1]

A number of imaging modalities exist to help diagnose coronary artery diseases. Among them, X-ray coronary angiography and intravascular ultrasound (IVUS) represent the most commonly used diagnostic tools. Selective coronary angiography provides projectional X-ray images of contrast-filled coronary vessels and has been clinically used for several decades. Although it provides detailed images of the vessel lumen, it offers no information about the coronary wall. IVUS is a relatively new technique that offers image information that is complementary to that provided by angiography. It generates cross-sectional images of the lumen, plaque, and vessel wall.

Segmentation of deformable structures is a common processing problem in medical imaging. For example, coronary artery atherosclerosis severity is mainly deduced from the degree of vessel stenosis induced by the atherosclerotic plaque formation.[1–3] This is generally estimated from IVUS images by segmenting and measuring the lumen area and by referencing it to the total cross-sectional area of the vessel. With the majority of IVUS systems, this work is generally performed manually. However, as manual tracing is time-consuming, many research groups have worked on developing semiautomatic and automatic segmentation and analysis methods in IVUS images as well as angiography.[1–11]

Brusseau et al.[7] developed a fully automatic method for luminal contour segmentation in IVUS images based on an active contour that evolves until it optimally separates regions with different statistical properties. Their system used a phase-array transducer and achieved a high level of accuracy. However, no mention was made of the widely used rotating systems.

Bovenkamp et al.[8] developed an automatic multiagent-based system for luminal contour segmentation. Each agent

E. dos Santos Filho (✉)
Graduate School of Engineering, Tohoku University, 6-6-5 Aoba, Aoba-ku, Sendai 980-8579, Japan
Tel. +81-22-795-7130; Fax +81-22-263-9488
e-mail: santos@yoshizawa.ecei.tohoku.ac.jp

M. Yoshizawa
Information Synergy Center, Tohoku University, Sendai, Japan

A. Tanaka
College of Symbiotic System Science, Fukushima University, Fukushima, Japan

Y. Saijo
Institute of Development, Aging and Cancer, Tohoku University, Sendai, Japan

T. Iwamoto
Graduate School of Engineering, Tohoku University, Sendai, Japan

cooperates with other agents to come to a consistent overall image segmentation. However, the complexity of this system may lead to time delays when there is a conflict among the agents.

Tuceryan[12] proposed a method for obtaining texture features directly from gray-level images by computing the moments of the image in local regions. The results of his segmentation algorithm show that the image moments computed over local regions provide a powerful set of features that reflect certain textural properties in images.

In this article, as in those by Brusseau et al.[7] and Bovenkamp et al.,[8] we propose a system for automatic luminal contour segmentation. Unlike the Brusseau et al. system,[7] our system is applied to images obtained from a rotating IVUS system because these systems are widely used in clinical settings. Instead of a multiagent system, as proposed by Bovenkamp et al.,[8] we used the simpler and more powerful set of features proposed by Tuceryan[12] to achieve our goal of luminal contour segmentation.

Our strategy to achieve this goal is to extract local moment-based texture features and a pixel position feature from IVUS images to perform a clustering on the basis of these features. Once we obtain the clustered image, a smoothing filter is applied to reduce the irregularities.

Materials and methods

Local moments have attracted attention as local features in applications such as edge detection and texture segmentation.[13–18] The main reason for this is that they are inherently integral-based features, so their use reduces the effect of uncorrelated noise. The computation of local moments, when viewed as a neighborhood operation, can be interpreted as a convolution of the image with a set of masks.[12] Tuceryan successfully proved the efficacy of local moments in texture segmentation.[12] However, in the case of luminal contour detection in IVUS images, an additional feature was necessary to take into account the concentric circular arrangement of artery layers. The feature used to carry this out was the radial distance.

Our texture segmentation algorithm is based on Tuceryan's work[12] and consists of the following steps:

Step 1: Compute the image moments within a small window around each pixel.
Step 2: Compute the texture features from the moments by applying a nonlinear transformation followed by an averaging operation.
Step 3: Compute the radial distance.
Step 4: For each pixel in the input image, compose a feature vector formed by features computed in step 2 and the radial distance computed in step 3.
Step 5: Perform a fuzzy clustering of the input image pixels on the basis of their feature vectors.
Step 6: Classify every pixel in the input image according to the minimum distance from the center of the clusters found in step 5.
Step 7: Perform morphological contour smoothing on the segmented image found in step 6.
Step 8: Find the final lumen contour by applying the Sobel operator[19] to the contour-smoothed image obtained in step 7.

Moments

Our algorithm uses the moments of an image to compute texture features. The $(p + q)$-th order moment m_{pq} of a function of two variables $f(x,y)$ with respect to the origin (0,0) is defined as[12]:

$$m_{pq} = \int_{-\infty}^{\infty}\int_{-\infty}^{\infty} f(x,y)x^p y^q dxdy \tag{1}$$

where $p, q = 0,1,2, \ldots$ Normally, the moments are computed over some bounded region. If the function is equal to unity within the region and zero outside the region, the lower order moments (small values of p and q) have well-defined interpretations. For example, m_{00} is the area of the region m_{10}/m_{00} and m_{01}/m_{00}, giving the x and y coordinates of the centroid for the region, respectively. The m_{20}, m_{11}, and m_{02} can be used to derive the amount of elongation of the region and the orientation of its major axis. The higher-order moments give even more detailed shape characteristics of the polygons such as symmetry.

In this article, as in Tuceryan's work,[12] we regard the intensity image as a function of two variables, $f(x,y)$. We compute a fixed number of the lower-order moments for each pixel in the image (we use $p + q \leq 2$). The moments are computed within a small local window around each pixel. Given a window size W, the coordinates are normalized to the range of $[-0.5, 0.5]$ and the pixel is located at the center. The moments are computed with respect to this normalized coordinate system, which permits us to compare the set of moments computed for each pixel. We always choose the window width W to be odd so that the pixel (i, j) is centered on a grid point.

Let (i, j) be the pixel coordinates for which the moments are computed. For a pixel with coordinates (k, l) that falls within the window, the normalized coordinates (x_k, y_l) are given by:

$$x_k = \frac{k-i}{W} \qquad y_l = \frac{l-j}{W} \tag{2}$$

Then the moment $m_{pq}(i,j)$ within a window centered at pixel (i, j) is computed by a discrete sum approximation of Eq. 1 that uses the normalized coordinates (x_k, y_l):

$$m_{pq}(i,j) = \sum_{k=-W/2}^{W/2}\sum_{l=-W/2}^{W/2} f(i+k, j+l)x_k^p y_l^q \tag{3}$$

This discrete computation of the set of moments for a given pixel over a finite rectangular window corresponds to a neighborhood operation, and, therefore, it can be interpreted as a convolution of the image with a mask.[12]

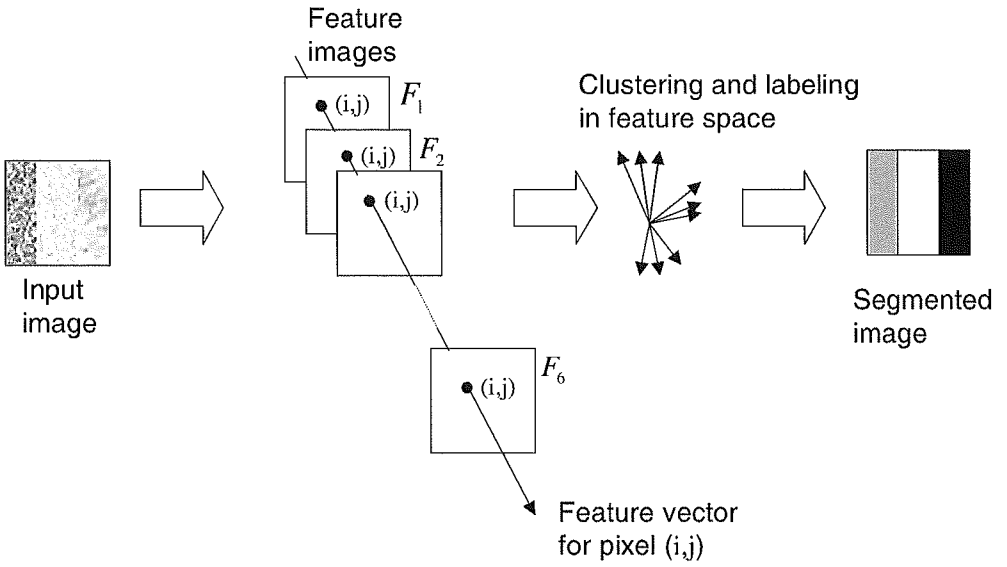

Fig. 1. Representation of a segmentation process on the basis of the feature images

When we examine these masks, we see that they can be interpreted as local feature detectors. For example, the mask for m_{00} corresponds to a box-averaging window, and thus it can be interpreted as computing the total energy within that box. The masks for m_{10} and m_{01} take the form of edge detectors. They would respond to sudden intensity changes in the x and y directions, respectively. The second-order moments are not easy to interpret; the only exception being m_{11}, which looks like a cross detector.[12]

The set of values for each moment over the entire image can be regarded as a feature image. Let M_k be the k-th such image. If we use n moments, then there will be n such moment images. In our experiments, we used up to second-order moments. That is, we used m_{00}, m_{01}, m_{10}, m_{11}, m_{02}, and m_{20}, which result in the images M_1, M_2, M_3, M_4, M_5, and M_6, respectively.

To enhance the discrimination power of these moments, we adopted the transformation used by Tuceryan.[12] Then, we introduced a nonlinear transducer that maps moments to texture features.

Thus, we obtain the texture feature image F_k corresponding to the moment image M_k with mean $\overline{M}$ using the following transformation:

$$F_k(i,j) = \frac{1}{L^2} \sum_{(a,b)\in\omega_{ij}} \left| \tanh\left(\sigma\left(M_k(a,b) - \overline{M}_k\right)\right)\right|; \qquad k = 1,2,\ldots,6 \tag{4}$$

where ω_{ij} is an $L \times L$ averaging window centered at location (i, j) and σ controls the shape of the function (we used $\sigma = 0.01$). Figure 1 shows a graphic representation of a segmentation process on the basis of the feature images.

The window size depends on the content of the image: finer textures require a smaller window size to detect smaller features, whereas coarser textures require a larger window. The parameters σ (in Eq. 4), moment window size W, and average window size L were chosen by gradually adjusting these values and observing the resultant effect in the segmented images. Initially, tests were done with increasing values of L for a fixed value W. Then, the fixed value W was increased and tested with increasing values of L. This process was repeated using the values 5, 7, 9, and 11 for W and L. Window sizes less than 5 were insufficient to capture the texture information, and sizes greater than 11 may lead to error in the contour definition. The choice of the best combination of values for W and L was based on visual evaluation of the resultant segmented images. After that, an adjustment of the parameter σ was made starting with the suggested[12] value 0.01. The range from 0.01 to 0.05 offered good results. The final chosen values were $W = 7$, $L = 9$, and $\sigma = 0.01$. They were determined empirically and are probably not optimal.

Luminal contour definition

The problem of luminal contour definition can be regarded as a clustering problem whose main point is to find features to each pixel of the IVUS image that could permit an accurate clustering and then to obtain a segmentation of regions of interest for physiologists such as the lumen, for example.

Due to the encouraging results obtained by Tuceryan,[12] the theory of moment-based texture segmentation was applied to the problem of luminal contour detection in IVUS images. The system proposed in this article can be represented in the block diagram shown in Fig. 2. The motivation for implementing this procedure for detection of the lumen boundary is that the IVUS images usually have very smooth gray-level transition between their regions and also there is noise. These facts make it difficult to detect the contour of the lumen region using only the traditional methods of edge detection such as Sobel and Canny operators[19,20] directly. An example is shown in Fig. 3. Thus, in the proposed system we identify the pixels that belong to the

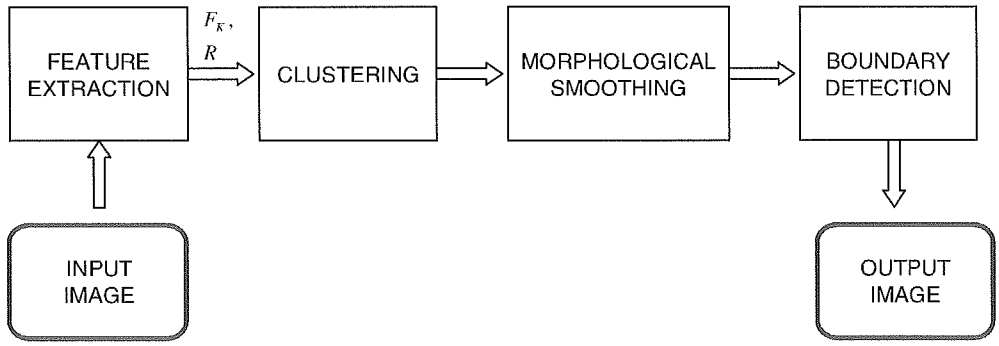

Fig. 2. Block diagram of the proposed system for luminal contour segmentation

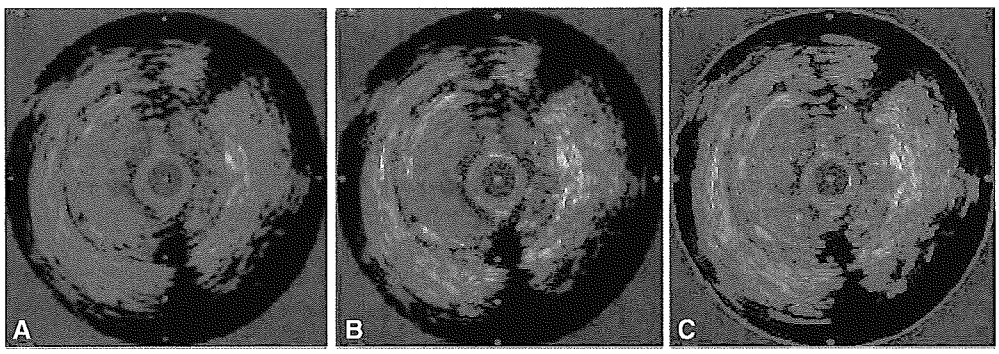

Fig. 3. Application of edge detection methods. **A** Original image. **B** Result of application of Sobel operator. **C** Result of application of Canny operator

lumen region through clustering based on their texture features and radial position feature. Then, we obtain images with regions well defined. After that we can easily detect the lumen contour using the traditional edge detection techniques.

Input image

In the proposed system (see Fig. 2), the input image is the original image obtained from the IVUS system. In this work, we used a commercially available IVUS system (Clear View Ultra; Boston Scientific, Natick, MA, USA). The central frequency of the rotating IVUS probe (Atlantis SR Pro; Boston Scientific) was 40 MHz.

Feature extraction

The feature extraction block is in charge of extraction of the transformed versions of the moments, F_k ; $k = 1, 2, \ldots, 6$, already defined, and the radial distance R is presented graphically in Fig. 4.

Examples of the moment images are shown in Fig. 5. Some vertical and horizontal elongated textures became slightly enhanced in the lumen region, especially in images M_4, M_2, and M_3, and more weakly in images M_5 and M_6. Image M_1 is a blurred version of the original image giving information about the average gray level. After application

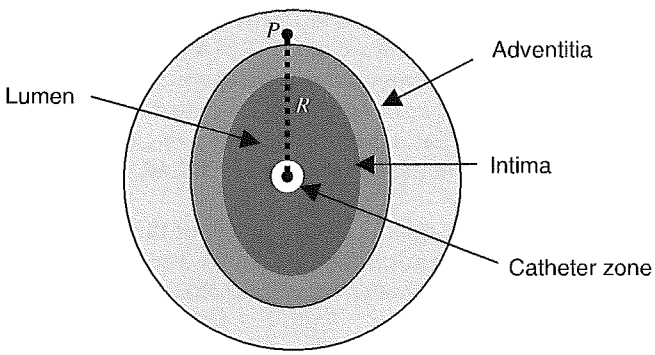

Fig. 4. Illustration of a cross section of a blood vessel. R, radial distance; P, pixel

of the nonlinear transformation (Eq. 4), these images became enhanced (Fig. 6). The lumen region became differentiated from the other regions, except in image F_1 that slightly enhanced the edges by computing the average gray level.

However, even after applying nonlinear transformation, these features were not sufficient to lead to reasonable lumen region segmentation. Then, the radial distance feature R was added to the clustering process.

In this work, we define the radial distance R as the distance from the central pixel of the image to the position of the pixel P under consideration. This distance R is normalized and becomes the seventh feature used in the following clustering of the input image pixels. The radial distance R is

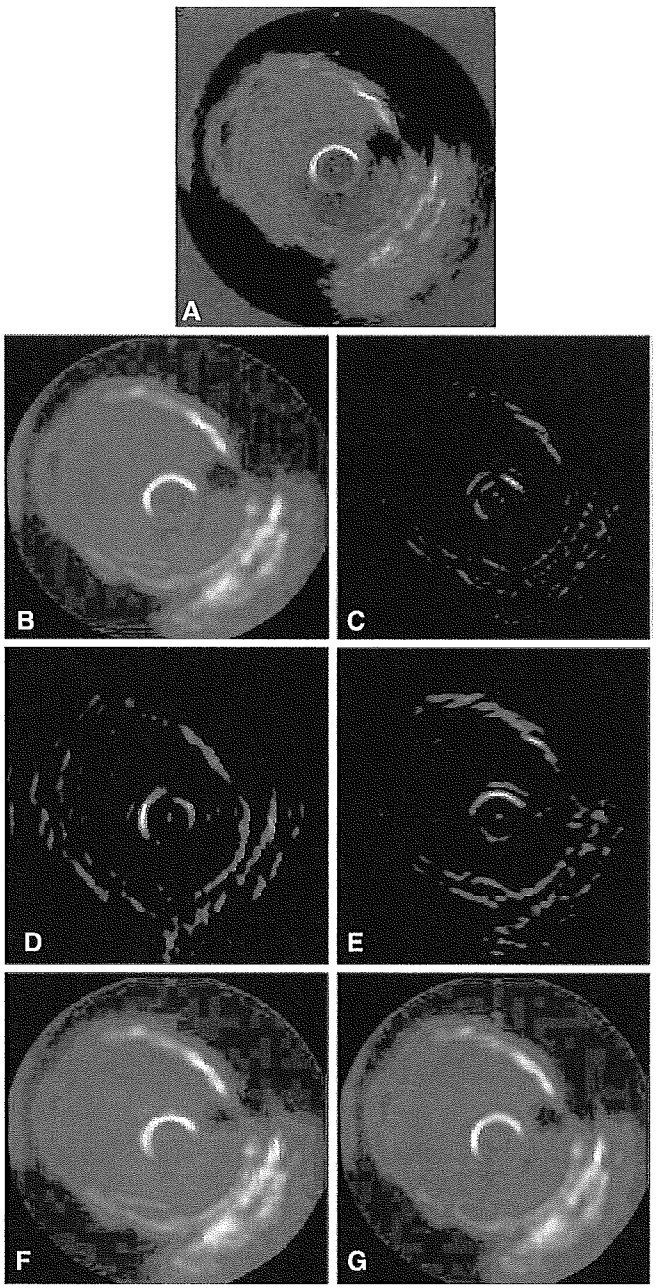

Fig. 5. Moment images. **A** Original image. **B** Moment image M_1. **C** Moment image M_4. **D** Moment image M_2. **E** Moment image M_3. **F** Moment image M_5. **G** Moment image M_6

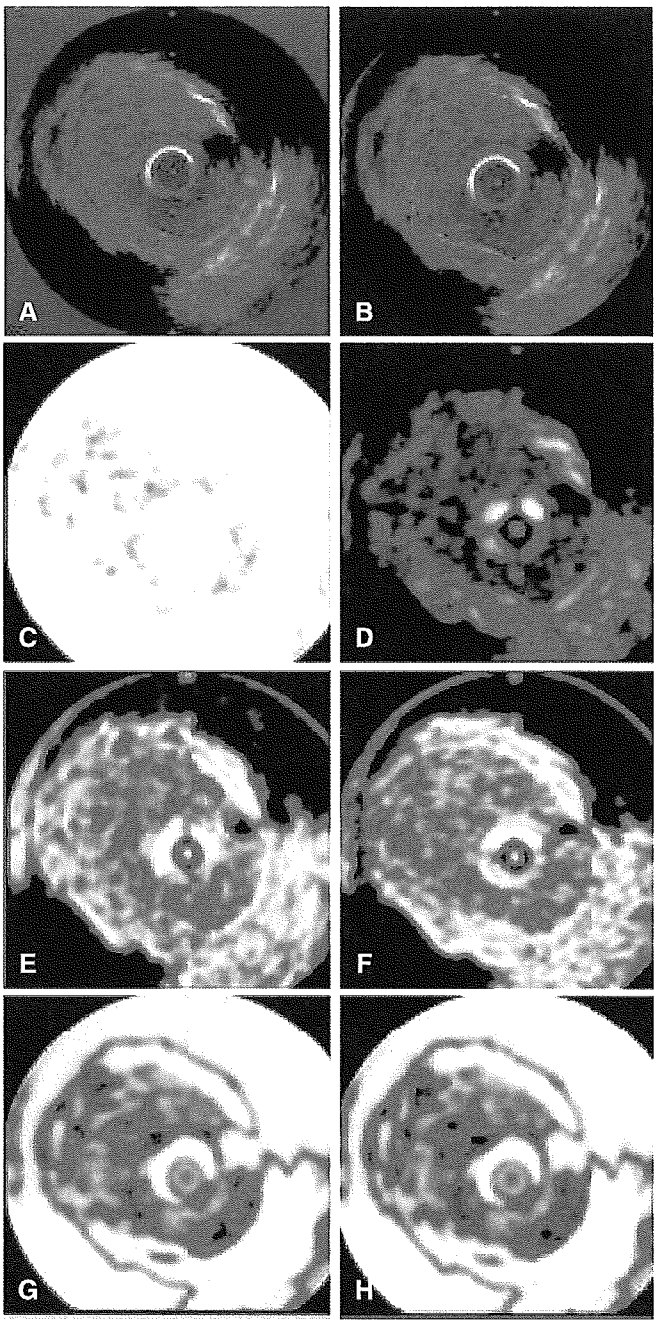

Fig. 6. Feature images. **A** Original image. **B** Final segmented image. **C** Feature image F_1. **D** Feature image F_4. **E** Feature image F_2. **F** Feature image F_3. **G** Feature image F_5. **H** Feature image F_6

of fundamental importance because it allows pixels that are at similar distance from the center of the image to be included in the same cluster if they have similar texture features. The effect of the use of these texture and position features is that the clusters become organized in regions similar to concentric rings around the center pixel; this is associated with the physiological structure of the blood vessels, as represented in Fig. 4. The effect of adding the radial distance feature R to the feature vector can be observed in Fig. 7. Thus, these seven features were used to comprise a feature vector for each pixel of the image.

Clustering

In this block we used the well-known Fuzzy C-Means[21] algorithm, which has been successfully utilized in several image processing applications in the field of medical imaging.[22] This clustering technique uses the feature vectors to distinguish the different regions of the image. Through successive iterations of an optimization routine, the central vector of each cluster is found. Then, the input image pixels are assigned to the cluster whose center vector is the closest to their feature vector. The number of clusters chosen was

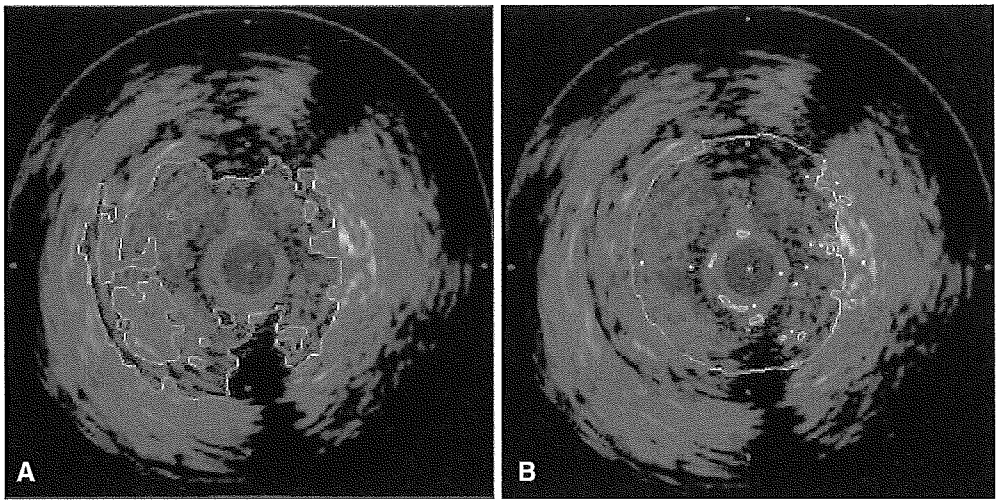

Fig. 7. Effect of the radial position feature R as one of the components of the feature vector. **A** and **B** are the same images obtained from patient A. **A** Clustered image without using the radial distance feature R. **B** Clustered image using the radial distance feature R

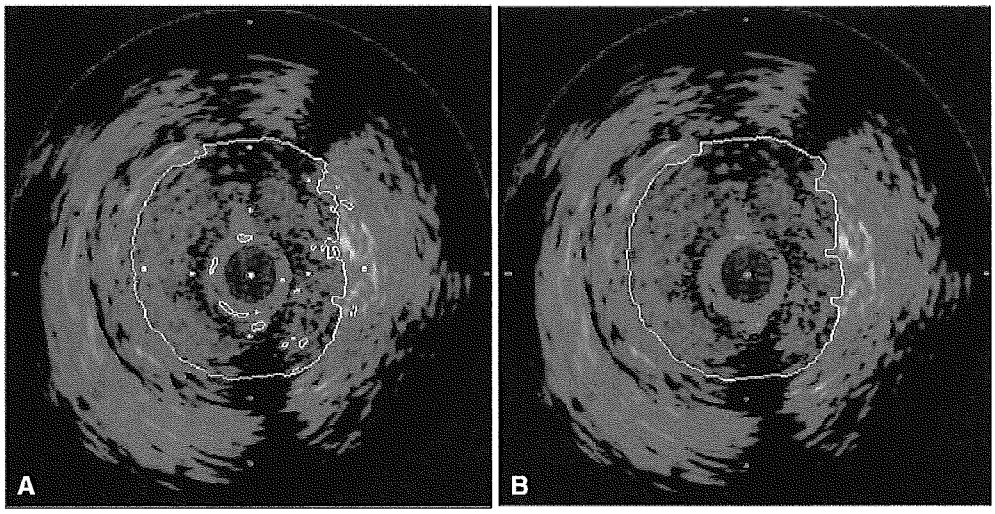

Fig. 8. **A** Result of clustering. **B** Result of morphological filtering

four: one cluster for the external region, one for the region between the adventitia and intima, one for the lumen, and another one for the catheter zone.

Morphological smoothing

Mathematical morphology is a technique of image processing whose value for each pixel in the output image is based on a comparison of the corresponding pixel in the input image with its neighbors. By choosing the size and shape of the neighborhood, we can define a morphological operation that is sensitive to specific shapes in the input image. The neighborhood size and shape are determined by the size and shape of a second, usually much smaller, image called a *structuring element*, which together with the input image is regarded as a set. Thus, basic operations of set theory, such as union, subtraction, and complement can be carried out with both images. These basic operations can be used to compose other operations, such as *opening* and *closing*.

Opening generally smoothes the contour of an object, breaks narrow isthmuses, and eliminates thin protrusions. Closing also tends to smooth sections of contour, but, as opposed to opening, it generally fuses narrow breaks and long thin gulfs, eliminates small holes, and fills gaps in the contour.[19]

To reduce the irregularities of the borders as well as some small regions around the borders, morphological filtering is done before boundary detection. This filtering is performed through the application of opening and closing morphological operations with a disk-structuring element of size 3. An example of the result of the luminal contour obtained only with the clustering process without any contour smoothing can be seen in Fig. 8A. An example of the luminal contour obtained when a morphological filter is applied after the clustering and before the boundary detection process is shown in Fig. 8B. Comparing these figures, we can observe that the morphological filter reduced the irregularities in the segmented contour and eliminated the small segmented regions.

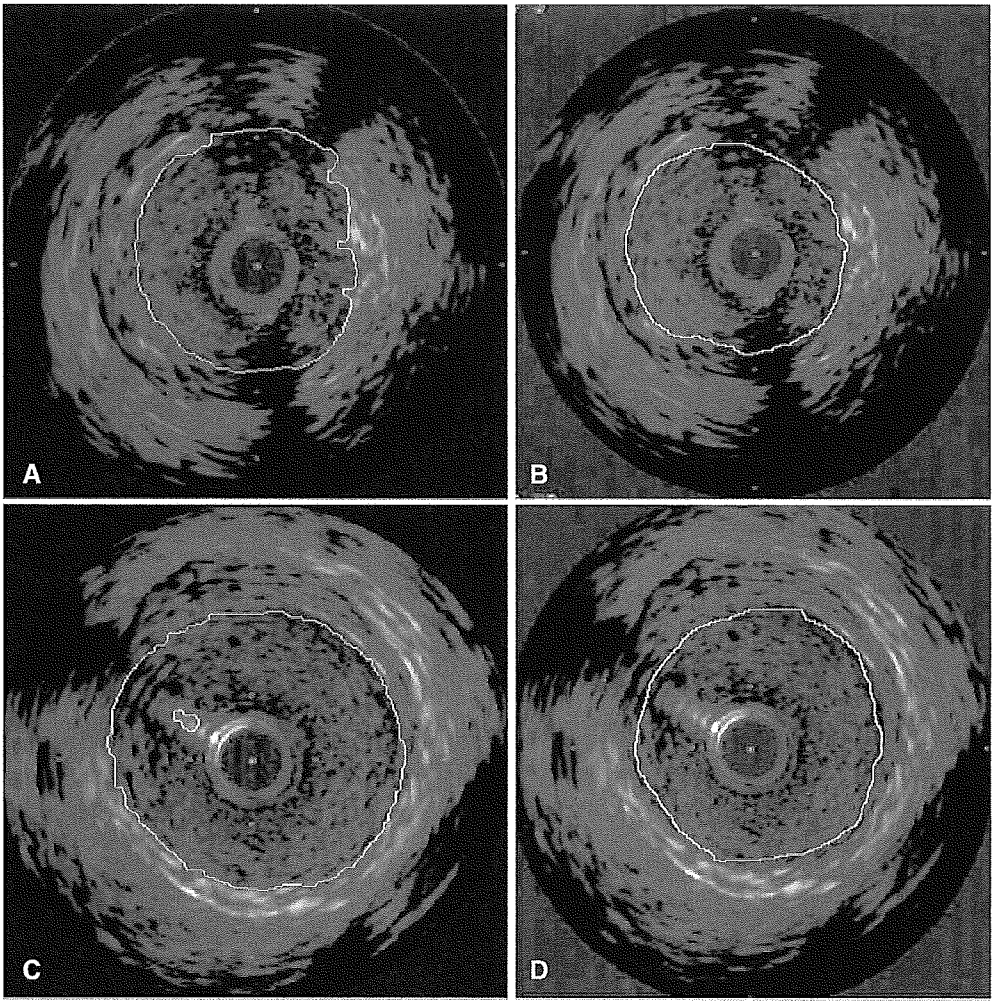

Fig. 9. Example of luminal contour detection. **A** and **B** are the same images obtained from patient A. **A** Automatically defined luminal contour. **B** Manually defined luminal contour. **C** and **D** are the same images obtained from patient B. **C** Automatically defined luminal contour. **D** Manually defined luminal contour

Boundary detection

After the clustering and contour smoothing, the images had well-defined regions, with contours that could easily be detected by traditional edge detection methods. In this system, we used the Sobel operator[19] because of its simplicity and efficiency. The Sobel operator performs a two-dimensional (2-D) spatial gradient measurement on an image, thereby emphasizing the regions of abrupt changes in gray level that correspond to edges.

Results

Using the system presented above, tests were done with 15 IVUS images of different patients. Cases with totally occlusive plaque and large shadow regions were not considered. Some examples of the results are shown in Fig. 9 together with the corresponding images that were segmented by a medical doctor for comparison.

We can see that the boundaries automatically drawn by the proposed system closely resemble those drawn manually by a medical doctor. However, some errors can be observed in the dark regions, in general caused by shadows that follow hard plaque or due to the guidewire. In these regions, the system tends to segment a region larger than that which would be segmented by a medical doctor; this occurs mainly because these dark regions contain no texture information and lead the system to be segment based only on the radial distance information. Thus, in the dark regions, the system tends to draw lines sometimes quite different from those drawn by a medical doctor (Fig. 10).

Sometimes bright regions appeared around the catheter zone, leading to a catheter cluster larger than the normal. However, as the size and position of the catheter are quite predictable, we can easily eliminate this effect in most of the images by compensating for the catheter cluster area.

The correlation between the areas of the automatically defined lumen and manually defined lumen is shown in Fig. 11. The correlation coefficient was equal to 0.86.

Discussion

The transition between the lumen and the vessel wall, as well as the transition between the vessel layers, is quite

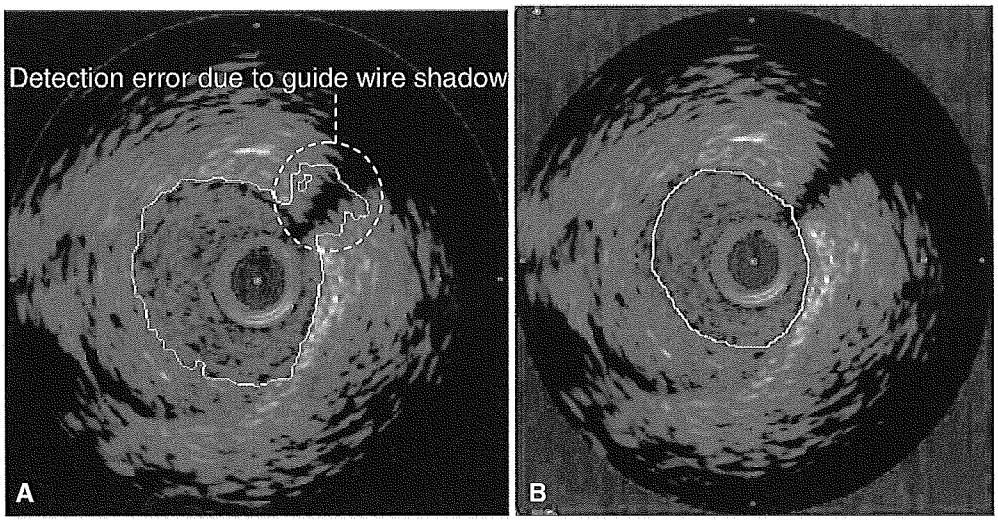

Fig. 10. Example of influence of guidewire shadow on the luminal contour detection process. **A** and **B** are the same images obtained from patient C. **A** Automatically defined luminal contour. **B** Manually defined luminal contour

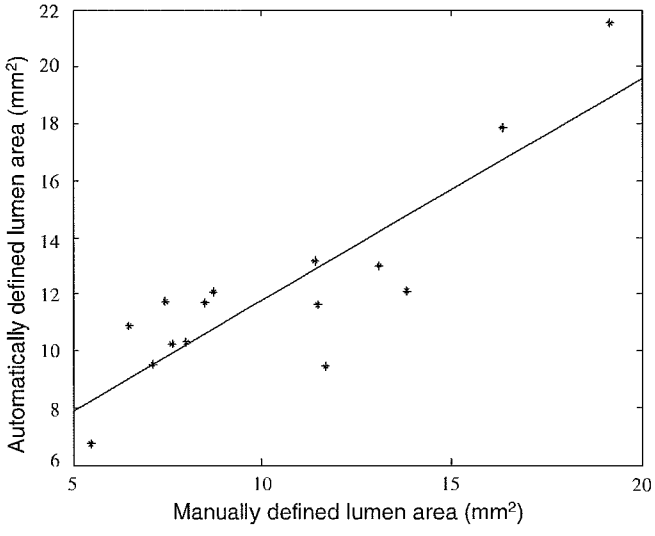

Fig. 11. Correspondence between lumen area manually defined and the same area automatically defined

smooth, making boundary detection based on local features a hard task. However, due to the ability of the local moment in distinguishing textured regions together with the radial distance, which is usually small in the lumen region, it was possible to overcome the difficulty caused by the smooth transition between regions. We can see that the automatically segmented image presented in Fig. 9A has a better luminal contour definition than the images yielded by the traditional methods presented in Fig. 3. We can also see that the automatically segmented images presented in Fig. 9 closely resemble the images manually segmented.

The effectiveness of the proposed radial distance feature R can be observed in Fig. 7. In Fig. 7A we see an example of segmentation without using the feature R. In this case, the resulting segmentation is more irregular and contains some subregions segmented inside the lumen region. This oversegmentation occurs mainly because of some texture and gray-level changes inside the lumen region. When the radial distance feature R is added to the clustering process, the differences among these segmented subregions is overcome because they acquire a feature that is similar in most of them, and then this strongly influences the clustering result. Thus, we can obtain a more regular and compact segmentation of the lumen region as shown in Fig. 7B.

In our tests, the moment-based texture features alone could not provide sufficient information for reasonably accurate lumen segmentation. The original contribution of this work is the combination of moment-based texture features with a position feature to comprise feature vectors for the clustering of IVUS images leading to reasonable segmentation of luminal contour.

However, the outer boundary of the vessel was not accurately detected, mainly because of the much smoother transition between the vessel external wall and the surrounding tissues. To overcome this difficulty, it seems that more global features need to be added to the system.

The problem of the error shown in Fig. 10A that is generated by the guidewire and shadowed area seems hard to solve using only these features based on moment and the radial distance because actually these regions contain no texture information. Thus, it seems that some kind of high-level knowledge needs to be introduced in the system to mimic human reasoning, as has recently been proposed by Bovenkamp with the multiagent system.[8] Another possibility is a previous elimination of the region shadowed by the guidewire from the image to be processed and, at the end, to make an interpolation to close the boundary found automatically.

Morphological smoothing could reduce the irregularities present in the detected contour. This technique proved to be useful in this application because it could efficiently eliminate the small unwanted segmented regions.

Luminal contour definition is also very useful in the process of plaque segmentation, as has been commented in a previous work.[23] The lumen boundary can be used to refine the space of search for plaque in an IVUS image

because the plaque always appears inside the walls of the vessel. Thus, the luminal contour can be used as an inner border of a region of search for plaque.

The delimitation of a region of search for plaque is especially important for systems whose identification method is based on clustering techniques and histograms. Elimination of the lumen region from the process of clustering also solves the problem of ring-down artifacts in the catheter zone that frequently appear as bright regions in IVUS images and sometimes influences the plaque segmentation process.

The window sizes depend on the content of the image: finer textures require a smaller window size to detect smaller features and coarser textures require larger windows. Thus, as the texture of the lumen region is finer than vessel wall texture, an adaptive method for adjustment of window size would probably be useful in the detection of the vessel contour.

Conclusions

In this article, an automatic algorithm dedicated to luminal contour segmentation in IVUS images has been introduced. This technique performs clustering of an input image on the basis of moment-based texture features and the radial distance.

Based on our tests, we can conclude that the moment-based texture features together with radial distance are feasible components for a feature vector in IVUS image segmentation when the aim is to find the luminal contour. However, some errors still occurred in the regions with shadows.

The process was improved when a morphological smoothing filtering was carried out after the clustering and before the boundary detection process. Tests performed with 15 images from different patients resulted in a correlation coefficient of 0.86 between the lumen areas automatically detected and the lumen areas manually detected.

Only the segmentation of the luminal contour has been considered. As future work, we plan to extend this method to detection of the vessel contour, which is necessary for assessment of the degree of vessel stenosis. In practical terms, once having determined the position of the blood-tissue interface, the luminal area will be excluded and the second contour will be searched in the remaining region.

References

1. Zhang X, Charles R, Sonka M. Tissue characterization in intravascular ultrasound images. IEEE Trans Med Imaging 1998;17:889–99.
2. Vince D, Dixon K, Cothren R, Cornhill J. Comparison of texture analysis methods for characterization of coronary plaques in intravascular ultrasound images. Comput Med Imaging Graphics 2000;24:221–9.
3. Solaiman B, Debon R, Pipelier F, et al. Information fusion: application to data and model fusion for ultrasound image segmentation. IEEE Trans BiomedEng 1999;46:1171–5.
4. Sonka M, Zhang X, Siebes M, et al. Segmentation of intravascular ultrasound images: a knowledge-based approach. IEEE Trans Med Imaging 1995;14:719–32.
5. Gronningsaeter A, Bjorn A, Heimdal A, et al. Vessel wall detection and blood noise reduction in intravascular ultrasound imaging. IEEE Trans Ultrasonics Ferroelectrics Freq Control 1996;43: 359–69.
6. Wink O, Niessen W, Viergever M. Fast delineation and visualization of vessels in 3D angiographic images. IEEE Trans Med Imaging 2000;19:337–46.
7. Brusseau E, Korte CL, Mastik F, et al. Fully automatic luminal contour segmentation in intracoronary ultrasound imaging – a statistical approach. IEEE Trans Med Imaging 2004;23:554–66.
8. Bovenkamp EGP, Dijkstra J, Bosch JG, et al. Multi-agent segmentation of IVUS images. Pattern Recog 2004;37:647–63.
9. Shiina T, Nitta N, Ueno E, et al. Real time tissue elasticity imaging using the combined autocorrelation method. J Med Ultrasonics 2002;29:119–28.
10. Ophir S, Alam SK, Garra BS, et al. Elastography: imaging the elastic properties of soft tissues with ultrasound. J Med Ultrasonics 2002;29:155–71.
11. Wang Y, Itoh K, Taniguchi N, et al. Studies on tissue characterization by texture analysis with co-occurrence matrix method using ultrasonography and CT Imaging. J Med Ultrasonics 2002;29: 211–23.
12. Tuceryan M. Moment based texture segmentation. Proceedings of 11th IAPR International Conference on Image, Speech, Signal Analysis and Pattern Recognition 1992:45–8.
13. The CH, Chin RT. On image analysis by methods of moments. IEEE Trans Pattern Anal Machine Intelligence 1988;10:496–513.
14. Khotanzad A, Hong YH. Invariant image recognition by Zernike moments. IEEE TransPattern Anal Machine Intelligence 1990;12: 489–97.
15. Martinez J, Thomas F. Efficient computation of local geometric moments. IEEE Trans Image Processing 2002;11:1102–11.
16. Sheynin S, Tuzikov A. Moment computation for objects with spline curve boundary. IEEE Trans Pattern AnalMachine Intelligence 2003;25:1317–22.
17. Yap P, Paramesran R. Image analysis by Krawtchouk moments. IEEE Trans Image Processing 2003;12:1367–77.
18. Suhling M, Arigovindan M, Hunziker P. Multiresolution moment filters: theory and applications. IEEE Trans Image Processing 2004;13:484–95.
19. Gonzales RC, Woods RE. In: Digital image processing. 2nd ed. New Jersey: Prentice Hall; 2002. p. 519–80.
20. Canny J. A computational approach to edge detection. IEEE Trans Pattern Anal Machine Intelligence 1986;8:679–98.
21. Bezdek JC. In: Pattern recognition with fuzzy objective function algorithms. New York: Plenum Press; 1981. p. 65–85.
22. Masulli F, Schenone A. A fuzzy clustering based segmentation system as support to diagnosis in medical imaging. Artif Intell Med 1999;16:129–47.
23. Santos Filho E, Yoshizawa M, Tanaka A, et al. An adaptive fuzzy segmentation of intravascular ultrasound images. Proc IEEE Int Symp Biomed Imaging 2004:1311–4.

Tokai J Exp Clin Med., Vol. 30, No. 4, pp. 217-225, 2005

Ultrasonic Tissue Characterization of Photodamaged Skin by Scanning Acoustic Microscopy

Muneo MIYASAKA, Shingo SAKAI*, Ayumi KUSAKA*, Yoko ENDO*, Masaki KOBAYASHI*, Kazuto KOBAYASHI**, Naohiro HOZUMI*** and Ryuzaburo TANINO

Department of Plastic Surgery, Tokai University School of Medicine
**Basic Research Laboratory, Kanebo Cosmetics Inc.,*
***Research & Development Dept., Honda Electronics Co., Ltd.,*
****Dept. of Electrical & Electronic Engineering, Toyohashi University of Technology*

(Received August 26, 2005; Accepted October 21, 2005)

The aim of this study was to ultrasonically characterize photodamaged skin of the elderly at the microscopic level using scanning acoustic microscopy which showed two-dimentional distribution of sound speed in the skin section. We confirmed that the expression level of the elastin gene was increased in the preauricular skin (photodamaged area), compared with postauricular skin (photo-protected area). The expression level of the procollagen gene was also increased in the preauricular skin compared with postauricular skin. The preauricular skin showed higher sound speed in the papillary dermis (Grenz zone). The site of progressive solar elastosis showed a somewhat sound speed velocity than that of the Grenz zone. Immunohistochemical staining showed conserved deposition of collagen in the Grenz zone even in the more photodamaged preauricular skin. These results suggest that fibrosis in the Grenz zone compensates tissue strength with the progress of solar elastosis. The sound speed analysis of skin will provide important information on heterogeneous mechanical changes in the skin during the process of photoaging.

Key words: ultrasound, scanning acoustic microscopy, sound speed, collagen, photoaging, papillary dermis

Abbreviations: SC, stratum corneum; SAM, scanning acoustic microscope; EVG stain, elastica van Gieson's stain; MMP, matrix metalloproteinase.

INTRODUCTION

Photoaging is distinguished from intrinsic aging and shows some distinctive histological alterations including enlargement and dysplasia of keratinocytes in the epidermis, solar elastosis and a mixed inflammatory infiltrate in the dermis [1]. In particular, the dermal degeneration such as collagen [2, 3], elastin [4] and basal membrane [5] degeneration cause a decrease in the elasticity of skin [6], and promote the formation of wrinkles. So far, skin elasticity has been measured as a total physical property of multilayers such as the stratum corneum, keratinocyte layer and the dermis. Even in the dermis, there are the differences in thickness of collagen fibers [7] and the direction of elastic fibers [8] from the papillary dermis to the reticular dermis, but the contribution of localized changes in the physical properties of the dermis to the whole-skin elasticity during photoaging remains obscure. It is also important to clarify localized changes of physical properties in the skin in the formation of wrinkles.

A scanning acoustic microscope (SAM) system has been used to determine quantitatively the ultrasonic properties of tissue at the microscopic level. Two-

Muneo MIYASAKA, Department of Plastic and Reconstructive Surgery, Tokai University School of Medicine, Bohseidai, Isehara, Kanagawa 259-1193, Japan Tel: +81-463-93-1121 Fax: +81-463-93-7231 E-mail: miyasaka@is.icc.u-tokai.ac.jp

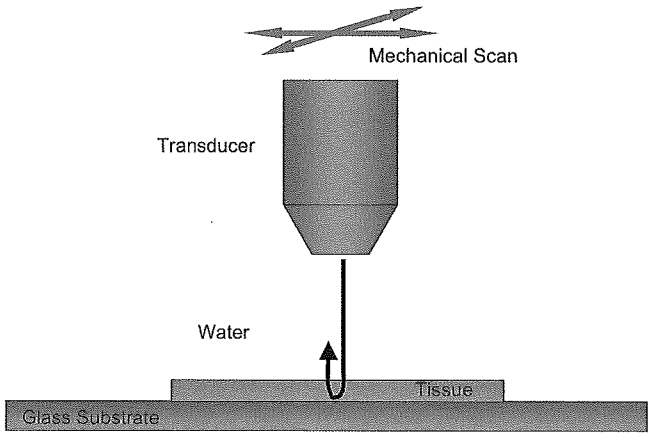

Fig. 1 Concept of ultrasonic microscopy for tissue characterization.

dimensional distribution of sound speed in microscopic sections can be obtained using the SAM system. The sound speed is considered to be mainly determined by the elastic property of tissue components on the assumption that biological tissue is fluid-like. In fact, Verdonk *et al.* [9] and Hoffmeister *et al.* [10] demonstrated that the velocity parallel to myocardial fibers was faster than the velocity perpendicular to the fibers. Saijo *et al.* reported high sound speed in fibrotic sites in the myocordium of patients with myocordial infarction [11]. However, measurement of the distribution of sound speed in the skin tissue using the SAM system has not been widely reported.

In this study, we ultrasonically characterize and compare a photodamaged skin section (preauricular area), and photo-protected skin (postauricular area but not buttock skin) using scanning acoustic microscopy, because regional differences in the structure of the skin have been reported [12].

MATERIALS AND METHODS

Biopsies

Eight Japanese volunteers (three men and five women; age range 66-83 years) were recruited for this study. Surgical biopsies were taken from both the preauricular skin and the postauricular skin of the same subject. The Tokai University Hospital Ethics Committee approved the study, and written consent was obtained from all subjects. Four healthy Caucasian female volunteers (age range 63-69 years) were also recruited. Punch biopsies (3 mm) were taken from the buttocks of each subject. Informed consent in writing was obtain from all subjects. Biopsy specimens were fixed in formalin, embedded in paraffin, sectioned to 10μm in thickness using a microtome, and deparaffinized for measurement using SAM.

Measurements By Scanning Acoustic Microscopy

Experimental setup

Figure 1 illustrates the concept of the ultrasonic microscope (HUM-1000, Honda Electronics Co., Ltd., Toyohashi, Japan) for tissue characterization. An acoustic wave is transmitted and received by the same transducer. Distilled water is used for the coupling medium between the specimen and the transducer. Reflections at both surfaces of the tissue are compared to measure the sound speed and thickness. Two-dimensional profiles of reflection intensity, thickness and sound speed can be obtained by mechanically scanning the transducer.

The transducer was 1.2 mm in aperture diameter, and 1.5 mm in focal length. Its nominal frequency range was 50-105 MHz (−6 dB), with a central frequency of 80 MHz. An acoustic wave with a wide frequency component was generated by applying the voltage pulse, and irradiated the substrate. The reflection was detected by the same transducer, and was introduced into the analog digital converter (ADC). The band limit and sampling rate were 500 MHz and 2.0 GS/s, respectively. In order to reduce random noise, eight of responses at the same point were averaged in the ADC before being introduced into the computer. The transducer

was mounted on an X-Y stage that was driven by the computer. Considering the focal distance and the cross sectional area of the transducer, the diameter of the focal spot was estimated to be 18μm at 80 MHz.

Analysis

The analysis for the pulse driven type microscopy is illustrated in Fig. 1 in comparison with the conventional burst driven type. The reflected wave is composed of the reflection at the front and rear surfaces of the tissue slice. In the pulse driven type, the reflected wave in the time domain is Fourier transformed into the frequency domain. Then the attenuation and phase spectra are compared with those of the direct reflection at the glass surface where no tissue is present. Because the signal is the result of the interference of two reflections, the attenuation spectrum has both maximum and minimum points as a function of frequency. Assuming fm as one of the minimum and maximum points, and ϕm as the corresponding phase angle, the phase lag between the above two reflections at the minimum point is $(2n-1)\pi$, giving

$$2\pi f_m \times \frac{2d}{c_0} = \phi_m + (2n-1)\pi \quad (1),$$

where d, co, and n are the tissue thickness, sound speed of the water, and a non-negative integer, respectively. The phase lag at the maximum point is $2n\pi$, giving

$$2\pi f_m \times \frac{2d}{c_0} = \phi_m + 2n\pi \quad (2).$$

The phase angle ϕm can be expressed by

$$2\pi f_m \times 2d\left(\frac{1}{c_0} - \frac{1}{c}\right) = \phi_m \quad (3),$$

since ϕm is the phase lag between the wave passing through distance 2d with sound speed c and that passing though the corresponding distance with sound speed co. From eqs. (1) and (3),

$$d = \{\phi_m + (2n-1)\pi\} c_0 / 4\pi f_m \quad (4)$$

is obtained. The thickness d can also be obtained from eqs. (2) and (3) as

$$d = \{\phi_m + 2n\pi\} c_0 / 4\pi f_m \quad (5).$$

The sound speed is subsequently obtained as

$$c = \left(\frac{1}{c_0} - \frac{\phi_m}{4\pi f_m d}\right)^{-1} \quad (6).$$

After the measurement, staining with elastica van Gieson's stain was performed.

Real-time PCR

The specimens for total RNA extraction were conserved in RNAlater (Ambion, Austin, TX). Total RNA was isolated from human skin samples using TRIzol reagent (Invitrogen Life Technologies, Carlsbad, CA) and RNeasy Mini Kit (Qiagen, Valencia, CA). cDNA synthesis was carried out with MessageSensor™ RT Kit (Ambion). Real-time PCR was performed on the ABI PRISM 7000 Sequence Detection System (Applied Biosystems, Foster City, CA) using TaqMan Gene Expression probes and TaqMan Universal PCR Master Mix (Applied Biosystems). Gene-specific primers (Assay ID) were as follows: Type I collagen α1 subunit (COL1A1), Hs00164004; Type I collagen α2 subunit (COL1A2), Hs00164099; and tropoelastin (ELN), Hs00355783. The quantity of PCR products was calculated from the cycle threshold value. The levels of gene expression were normalized with those of the GAPDH gene.

Statistical analysis was performed using the Wilcoxon signed-rank test.

Immunohistochemical staining

Paraffin-embedded biopsies were sectioned (5μm), deparaffinized, ethanol-rehydrated, subjected to antigen retrieval, and rinsed with PBS. Nonspecific antibody binding was blocked by incubating the sections for 10 min in Protein Block Serum-Free (X0909, DAKO, Glostrup, Denmark). Blocked sections were incubated for 1 h with anti-collagen I (ab292, Abcam, Cambridge, UK) or anti-elastin (PR533, Elastin Products Company, MO, USA) in 1% BSA/PBS. The sections were then rinsed four times with PBS and incubated for 1 h with Fluorescein(FITC)-conjugated goat anti-rabbit IgG (111-095-144) or Cy3-conjugated goat anti-rabbit IgG (111-165-144, Jackson ImmunoResearch Laboratories, PA, USA). The slides were then sealed using SlowFade Antifade Kit (S-2828, Molecular Probes, OR, USA). The slides were examined by a laser scanning confocal microscope (Carl Zeiss LSM510, Jena, Germany).